Postnatal Development of Chorda Tympani Axons in the Rat Nucleus of the Solitary Tract

Siting Wang, James Corson, David Hill, and Alev Erisir*
University of Virginia, Charlottesville, Virginia 22904

ABSTRACT

The chorda tympani nerve (CT), one of three nerves that convey gustatory information to the nucleus of the solitary tract (NTS), displays terminal field reorganization after postnatal day 15 in the rat. Aiming to gain insight into mechanisms of this phenomenon, CT axon projection field and terminal morphology in NTS subdivisions were examined using tract tracing, light microscopy, and immunoelectron microscopy at four postnatal ages: P15, P25, P35, and adult. The CT axons that innervated NTS rostrolateral subdivision both in the adult and in P15 rats were morphologically distinct from those that innervated the rostrocentral, gustatory subdivision. In both subdivisions, CT terminals reached morphological maturity before P15. Rostrolateral, but not rostrocentral axons, went through substantial axonal branch elimination after P15. Rostrocentral CT synapses, however, redistribute onto postsynaptic targets in the following weeks. CT terminal preference for GABAergic postsynaptic targets was drastically reduced after P15. Furthermore, CT synapses became a smaller component of the total synaptic input to the rostrocentral NTS after P35. The results underlined that CT axons in rostrocentral and rostrolateral subdivisions represent two distinct populations of CT input, displaying different morphological properties and structural reorganization mechanisms during postnatal development. J. Comp. Neurol. 520:3217–3235, 2012.

INDEXING TERMS: development; chorda tympani; gustatory; taste; electron microscopy

The chorda tympani nerve (CT) is a branch of the facial nerve, conveying sensory information originating from the fungiform papillae located on the anterior third of the tongue and the anterior foliate papillae located on the posterior tongue to the nucleus of tractus solitarii (NTS) (Whiteside, 1927). While a major termination site for these axons is in the gustatory, rostrocentral subdivision of the NTS, which contains cells that project to the waist region of the parabrachial nucleus (Norgren and Leonard, 1973; Norgren, 1978; Whitehead, 1990; Halsell et al., 1996; Halsell and Travers, 1997), the CT also sends a substantial projection to the rostrolateral and caudal ventrolateral subdivisions (Whitehead et al., 1999; Corson et al., 2012). Developmentally, an adult-type terminal field pattern emerges in rat between postnatal days (P)15 and 60, during which initially widespread and dense CT projections gradually become more compact (King and Hill, 1991; Krimm and Hill, 1997; May and Hill, 2006; Sollars et al., 2006; Mangold and Hill, 2007, 2008). As this development also coincides with a similar reorganization of greater superficial petrosal (GSP) and glossopharyngeal (IX) inputs terminating in distinct yet overlapping regions of NTS (May and Hill, 2006; Mangold and Hill, 2007, 2008), competitive influences among orosensory afferent fibers to NTS are deemed important in instructing axon branch retraction, synapse pruning, and thus terminal field formation (Corson and Hill, 2012).

Competitive pruning of initially exuberant developing axons is a common strategy for establishing proper functional connections, and provides a substrate for neural plasticity in developing primary sensory and motor inputs. Developmental stages of axon elimination are encountered in many systems including neuromuscular junction motor afferent innervation (Colman et al., 1997; Kasthuri and Lichtman, 2003), retinogeniculate segregation (Katz and Shatz, 1996; Penn and Shatz, 1999; Demas et al., 2006; Ziburkus and Guido, 2006), and sensory map

Grant sponsor: National Institutes of Health (NIH); Grant numbers: NIH-NIDCD 1R01 DC010183 (to A.E.), NIH-NIDCD R01 DC00407 (to D.H.).

*CORRESPONDENCE TO: Alev Erisir, PO Box 400400, Charlottesville, VA 22904. E-mail: erisir@virginia.edu

Received February 16, 2011; Revised September 12, 2011; Accepted March 14, 2012
DOI 10.1002/cne.23093
Published online March 20, 2012 in Wiley Online Library (wileyonlinelibrary.com)

formation (O'Leary et al., 1990, 1992; McLaughlin et al., 2003; Kamiyama et al., 2006; Inan and Crair, 2007). In those systems, synapse pruning is instrumental in elimination of polyneuronal convergence, which may underlie Hebbian-type interactions in determining lifelong targets of sensory afferent fibers. Furthermore, this competitive pruning occurs while the axons are still in the early stages of their maturation. These exuberant synapses are morphologically immature (Campbell and Shatz, 1992; Sanes and Lichtman, 1999; Kasthuri and Lichtman, 2003), and the elaboration of synapse number and morphology continues after the pruning stages are completed (Luo and O'Leary, 2005).

Aiming to gain insight into the mechanisms of developmental CT axonal reorganization, we tested the hypothesis that CT axonal pruning between P15 and adult in the rat NTS coincides with a stage of morphological maturation similar to mechanisms observed in other systems in the vertebrate brain. Further, we determined whether any differences exist between the CT axons that are located in regions from which major axon retraction occurs after P15 and those that continue to receive the majority of CT input. In order to test these hypotheses, we examined subdivision specificity for axon retraction and the morphological properties of CT terminals and their postsynaptic targets at four postnatal ages (P15, P25, P35, and adult) at both the light and electron microscopic levels.

MATERIALS AND METHODS

All data were obtained from 28 Sprague–Dawley rats (Harlan, Indianapolis, IN) at P15 ($n = 10$; included animals at P15 or P16), P25 ($n = 4$), P35 ($n = 4$), and adult (P60 or older; $n = 10$). Three of the adult animals were also used in a previous light microscopy study (Corson et al., 2012). All animal procedures were performed in accordance with National Institutes of Health (NIH) guidelines for humane handling of animals and all protocols were approved by the Institutional Animal Care and Use Committee at the University of Virginia.

Tracer application and tissue preparation

Rats were maintained on a standard diet throughout the experiments and nerve-labeling surgeries were performed at each designated age. For application of tracers, each animal was anesthetized with medetomidine/ketamine (0.2, 20 mg/kg; intramuscularly [IM]), and placed on a water-circulating heating pad to maintain body temperature. A nontraumatic head holder (Erickson, 1966) was used to stabilize the animal and the ventral surface of the neck incised. Blunt dissection of muscle and connective tissues allowed access to the tympanic bulla (Sollars and Hill, 2005), in which a small hole was made to expose the CT. The CT was then cut peripheral to the ganglia and crystals of 3 kD biotinylated dextran amine (BDA, Invitrogen, Carlsbad, CA) were placed on the proximal end of the nerve. The incision was then sutured and the rat was injected with atipamezole (IM, 1.6 mg/kg) to reverse the anesthesia. Following 48-hour survival time, each rat was deeply anesthetized with urethane (3 g/kg) and transcardially perfused with Tyrodes Buffer (137 mM NaCl, 5.5 mM dextrose/glucose, 1.2 mM $MgCl_2$, 2 mM KCl, 0.4 mM NaH_2PO_4, 0.9 mM $CaCl_2$, 11.9 mM $NaHCO_3$, in 1 L dH_20; pH 7.3) at room temperature, followed by either 4% paraformaldehyde (for light microscopy) or a mixture of 4% paraformaldehyde and 1% glutaraldehyde (for electron microscopy) in 0.1 M phosphate buffer (PB, pH 7.4). The brains were removed and postfixed in the same fixative overnight. The medulla was then blocked and sectioned either horizontally or coronally on a vibratome (Leica VT1000S) at 50-μm thickness. Sections were collected in phosphate-buffered saline (PBS; 0.01 M PB + 0.9% NaCl; pH 7.4) at room temperature, then reacted with 1:100 avidin-biotin peroxidase complex (ABC; Vector, Burlingame, CA) in PBS overnight at 4°C. For sections that were examined only with the light microscope, 0.1% Triton X-100 was added to the ABC solution. Following 3 × 3-minute rinses in PBS, all sections were treated with 0.06% diaminobenzidine (DAB) and 0.01% H_20_2 in PBS for 5–12 minutes. Sections were then either mounted onto subbed glass slides for light level analysis or prepared for electron microscopy.

Light microscopy

Five P15 and three adult brains were used for light microscope identification of CT terminal fields within NTS subdivisions. For this, brains were sectioned coronally in three series. Two of the series were immediately mounted on subbed glass slides and were processed for either Nissl or myelin staining. The sections from the third series were collected and maintained in multiwell culture plates throughout ABC and DAB processing, after which they were mounted onto subbed glass slides, dehydrated, and coverslipped. Thus, we were able to preserve the serial order of all sections through NTS, stained with three different markers (Nissl, myelin, and CT axons), as described in detail previously (Corson et al., 2012). Briefly, one series was stained for Nissl using standard procedures with cresyl violet. The myelin stain was performed using a previously established gold chloride method (Schmued, 1990; Schmued and Slikker, 1999) with modifications. Sections were rehydrated in PBS and stained for 15–30 minutes in 0.2% gold hydrochloride ($HAuCl_4$ in 0.02 M PBS, pH 7.4) at 60°C followed by 2–3 minutes in 0.2% gold potassium chloride ($KAuCl_4$ in 0.9% NaCl) also at 60°C. Staining was determined to be

complete when fine black myelinated fibers were observed in the lateral NTS and sections were stained uniformly. The slides were then rinsed 2 × 2 minutes in PBS and incubated for 3 minutes in 1% sodium thiosulfate at 60°C, followed by rinses in PBS, dehydration, and coverslipping. The sections containing NTS were photographed at 5×, 20×, or 40× magnifications using a Leica DC200 camera. Adjacent myelin, Nissl, and CT-labeled sections were overlaid with Photoshop and Illustrator (Adobe, San Jose, CA), and structural borders and landmarks from myelin and Nissl were transposed onto the adjacent CT-labeled section.

Electron microscopy

DAB-stained sections (coronal or horizontal sections) were incubated in 1% osmium tetroxide in PB for 1 hour and in 4% uranyl acetate dissolved in 70% ethanol for 2–18 hours. They were then dehydrated sequentially in increasing concentrations of ethanol and acetone (EM grade, Electron Microscopy Sciences, Fort Washington, PA, EMS). Sections were then treated with 50/50 acetone/resin (EMBED812; EMS) for 2 hours, followed by full resin overnight. Sections were placed between two acetate sheets and cured in a 60°C oven for 1–2 days. These flat-embedded sections were examined with a light microscope to detect DAB-labeled CT projection fields in the rostral NTS; tissue landmarks and the labeled region were drawn with a camera lucida. The regions of interest were further trimmed and repolymerized at the bottom of BEEM capsules. The features of capsule-embedded sections were sketched in detail and the block was trimmed to a 2 × 1 mm trapezoidal block that spanned the NTS mediolaterally and contained the CT-labeled region. In horizontal sections the trapezoid typically contained the densest CT label field. In coronal sections the trapezoid contained either both the rostrocentral and rostrolateral subdivisions, or it contained the ventrolateral subdivision of the caudal NTS. Using a Leica Ultracut UCT, ultrathin sections (70–90 nm) were cut at a plane near-parallel to the surface of thick vibratome sections. This approach ensures that the top 5–10 μm of thick vibratome sections, where immunolabeling is present, are sectioned to yield a wide (100–200 μm) strip of labeled ultrathin tissue, called the tissue–resin interface. Sections were collected on 200-mesh nickel grids.

Postembedding GABA immunostaining

Previously published methods were used to achieve GABA labeling in postembedded tissue (Phend et al., 1992; Bickford et al., 1994; Erisir et al., 1997). Briefly, after ultrathin sectioning grids containing sections through tracer-labeled region of NTS were rinsed in 0.05 M Tris buffer with 0.9% NaCl and 0.1% Triton X-100 (TBST, pH 7.6), and subsequently placed under droplets of a 1:1,000 to 1:2,000 dilution of rabbit anti-GABA antibody (Sigma Chemical Company, St. Louis, MO; A#2052) in TBST overnight. The immunogen used to produce the GABA antibody was GABA-bound to bovine serum albumin (BSA). The GABA antibody shows positive binding with GABA and GABA-keyhole limpet hemocyanin, but not BSA, in dot blot assays (Sigma product information). Postembedding staining produced secondary binding that showed selectivity to only a portion of neuropil profiles, and it resulted in background gold binding that is comparable to previously published work using the same antibody (Brown et al., 2000; Erisir and Dreusicke, 2005; Bickford et al., 2010; Wang and Bradley, 2010; also see Tamamaki et al., 2003, who demonstrated specificity of this antibody in GAD67-containing cells). After primary antibody incubation, the sections were rinsed in TBST and incubated in 1:25 dilution of goat antirabbit IgG conjugated to 15-nm gold particles (Amersham, Arlington Heights, IL) in TBST for 1 hour. Uranyl acetate (4%) or lead citrate (2%) counterstaining was applied for contrast.

EM data collection from tracer-labeled tissue

Ultrathin sections were examined on a JEOL 1010 electron microscope. Consistent anterograde tracer labeling was found within 100 μm from the tissue–resin transition line and data collection was limited to a 5–50-μm wide strip at the tissue–resin interface. A 16 M pixel digital camera (SIA-12C, Scientific Instruments and Applications, Duluth, GA) was used to capture images at 8,000× or 12,000× magnification. For analysis of CT synapse volumetric density (Nv, see below), images from near-adjacent regions were made into a montage to form a composite of a uniformly stained expanse of tissue. Images were examined at about 50,000× final screen magnification and several measurements were taken using Image Pro Plus (v. 5.1, Media Cybernetics, Silver Spring, MD). The total area of neuropil appearing in the images (A) was calculated by excluding the areas occupied by cell somata, blood vessels, and myelinated axons. The average area of neuropil examined from each brain was 1.14 $\pm$ 0.02 $\times$ 10^3 μm^2. Within each composite area the following profiles were identified: 1) labeled profiles (anterogradely labeled CT fibers) that displayed a synapse at the cross-section; 2) labeled profiles without a synapse; 3) unlabeled profiles with a synapse; 4) profiles that were postsynaptic to labeled terminals with a synapse. From these profiles the following measurements were taken: i) synapse length of labeled terminal with a synapse (SL_l), and synapse length of unlabeled terminals (SL_u); ii) area of synaptic terminal (TA_l); iii) minimum (C_{minL}) and maximum (C_{maxL}) calibers of labeled profiles; iv) minimum caliber (C_{min}) of profiles postsynaptic to labeled terminals; v)

number of synapses formed by labeled terminals (N_{sL}) and by all terminals (N_s). We used counting methods and correction for synapse size bias, as done previously by us and others (DeFelipe et al., 1999; Erisir and Harris, 2003; May et al., 2007).

The estimated total axon length (L_{Ax}) was calculated using a previously described quantification approach (Erisir and Dreusicke, 2005; May et al., 2007). For this, the formula, $\Sigma[(C^2_{maxL}\text{-}C^2_{minL})^{0.5}+t]$, was applied, where t is the thickness of the ultrathin section (70 nm). This calculation yields an estimate of total axon length represented by the cross-sections of labeled axon within the examined area. This measure is then applied to calculate areal axon density (L_{Ax}/A) and axon synapsing frequency (N_{sL}/L_{Ax}). Volumetric density of labeled synapses (Nv_L) was also calculated using a previously described quantification approach (N_{sL} / [A * L_{sL}]; DeFelipe et al., 1999; Erisir and Harris, 2003). A similar formula was applied (N_s / [A_t * L_s]) to compute volumetric density of all synapses (labeled and unlabeled, Nv; L_s denotes the average length of all synapses) within the analyzed region. The use of volumetric density rather than simple area density measurements aims to eliminate the sampling biases that may occur in data collection strategies in which sampled units (in this case, synapses) are larger than the tissue thickness, and variables (labeled vs. all synapses) may have different thicknesses, thereby having different sampling probabilities. The ratio of all synapses within a given region that are formed by CT axons was then obtained.

Data collection from anterograde tracer and GABA-labeled tissue

Ultrathin sections containing DAB-labeled CT terminals and gold-labeled GABAergic dendrites and axons were analyzed. All synaptic contacts made by labeled terminals and their postsynaptic targets were photographed at 8,000× magnification. Images were examined using Image Pro Plus, and the areas of postsynaptic profiles as well as the number of gold particles contained therein were measured to calculate a gold density index (number of gold / area of profile) for each postsynaptic profile. The value for background gold density was determined in DAB-negative presynaptic profiles that formed asymmetric synapses (thus, presumed GABA-negative). The top 95th percentile gold density obtained from morphologically non-GABAergic profiles was used as the criterion for GABA positivity; that is, the minimum gold density for GABA+ classification. This criterion approach ensures eliminating the variability that may arise from immunostaining conditions of each brain, and it is not affected by the variability of GABA amount in different neurons and at different ages. The gold density index was also determined in DAB-negative (non-CT) terminals that made a synapse on the same postsynaptic profile as the DAB-positive (CT) terminal.

Statistical analysis

Statistical comparisons among the four age groups were performed by analysis of variance (ANOVA). Post-hoc comparisons were accomplished with least significant difference (LSD) tests, unless the variances were not homogeneous, which was determined by the Levene test. The variances were not homogeneous for tests of axonal density, total volumetric density, and synaptic length. For these tests, post-hoc comparisons were performed with Dunnett's T3 test. For comparisons of frequency distributions of pooled populations, nonparametric Kruskal–Wallis and Mann–Whitney *U*-tests were used. A chi-square test was used to examine the synaptic frequency of CT terminals across different ages. The alpha level of 0.05 was used to determine statistical significance.

RESULTS

Light microscopic characterization of CT projections

BDA placed at the cut nerve resulted in labeling of CT axons in the NTS at all ages examined. Superior salivatory nucleus cells, which innervate the parasympathetic submandibular ganglion via CT, were also retrogradely labeled in all cases. In order to determine the subdivisional localization and spread of CT labeled axons within NTS, we examined the entire brainstem stained for BDA (CT axons), myelin, and Nissl on adjacent sections (Fig. 1). As also described in our previous work (Corson et al., 2012), this allowed the identification of NTS subdivision borders on tracer-labeled tissue, and for the construction of complete sequences of tracer-labeled areas on a coordinate plane anchored at the anterior-most aspect of area postrema. The myelin stain allowed clear identification of the course of the solitary tract and dorsal and medial borders of the nucleus in both adult and P16 animals (Fig. 1B,E). The pattern of myelinated axon bundles of reticular formation tentatively defined the ventral border of the NTS at both ages, although in P15 brains the reticular formation myelination seems to still be in progress. The border between rostrocentral and rostrolateral subdivisions was identified based on the dense network of unbundled myelinated fibers, as described in Corson et al. (2012); this criterion was also useful in P15 animals. Nissl-stain-based criterion for the rostrocentral–rostrolateral border (smaller, densely packed, round or elongate cells in rostrocentral subdivision vs. sparse cells with pale cytoplasm in rostrolateral subdivision) was more useful in adult than P15 animals. The criterion landmark to identify the dorsal border of the ventral subdivision (i.e., anterior-

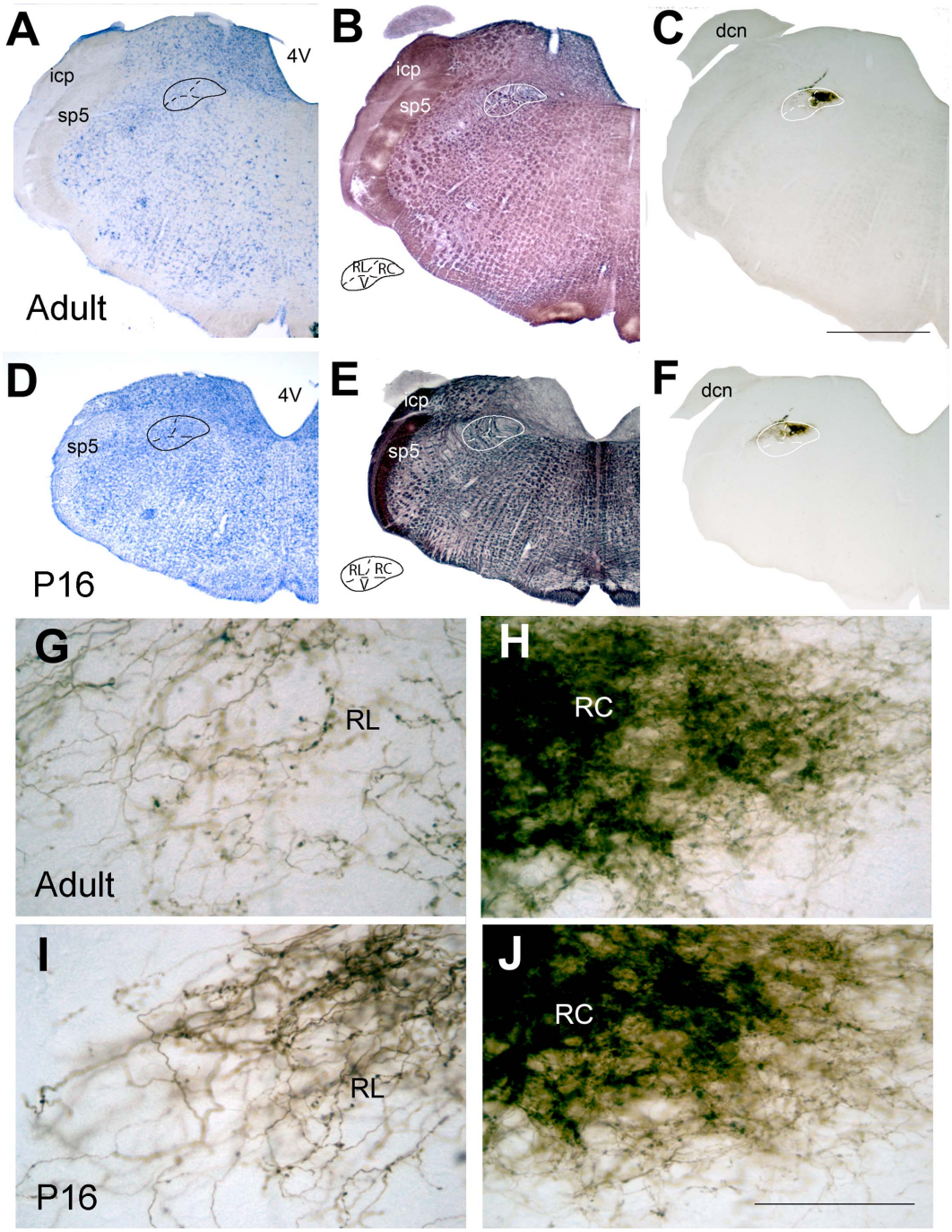

Figure 1. Identification of NTS, its subdivisions and CT projection fields in an adult (**A–C,G,H**) and a P16 **(D–F,I,J)** brain. Adjacent coronal sections through rostral NTS, stained for Nissl (A,D), myelin (B,E), or ABC-DAB for tract-tracer in CT fibers (C,F). NTS and subdivision borders (insets in B,E) were identified on myelin and Nissl sections and transposed on adjacent tracer labeled sections. G–J: Higher-magnification views of CT labeled sections in C (adult) and F (P16). DAB labeled, fine CT fibers densely filled the rostrocentral subdivision (H,J), while thicker yet sparser fibers were noted in the rostrolateral (G,I) subdivision at both ages. RC, rostrocentral; RL, rostrolateral; V, ventral subdivision; 4V, fourth ventricle; sp5, spinal trigeminal tract; icp, inferior cerebellar peduncle; dcn, dorsal cochlear nucleus. Scale bars = 1000 μm in C (applies to A–F); 125 μm in J (applies to G–J).

posteriorly coursing myelinated bundles within NTS proper) was distinct in both adult and P15 brains.

Qualitative appearance of tracer labeled fibers in rostrocentral and rostrolateral subdivisions were remarkably similar in adult and P15 brains (Fig. 1G–J). Compared to adult brains, coronal sections from P15 brains were noticeably smaller than those from adult brains, yet the NTS dimensions at mediolateral and dorsoventral aspects

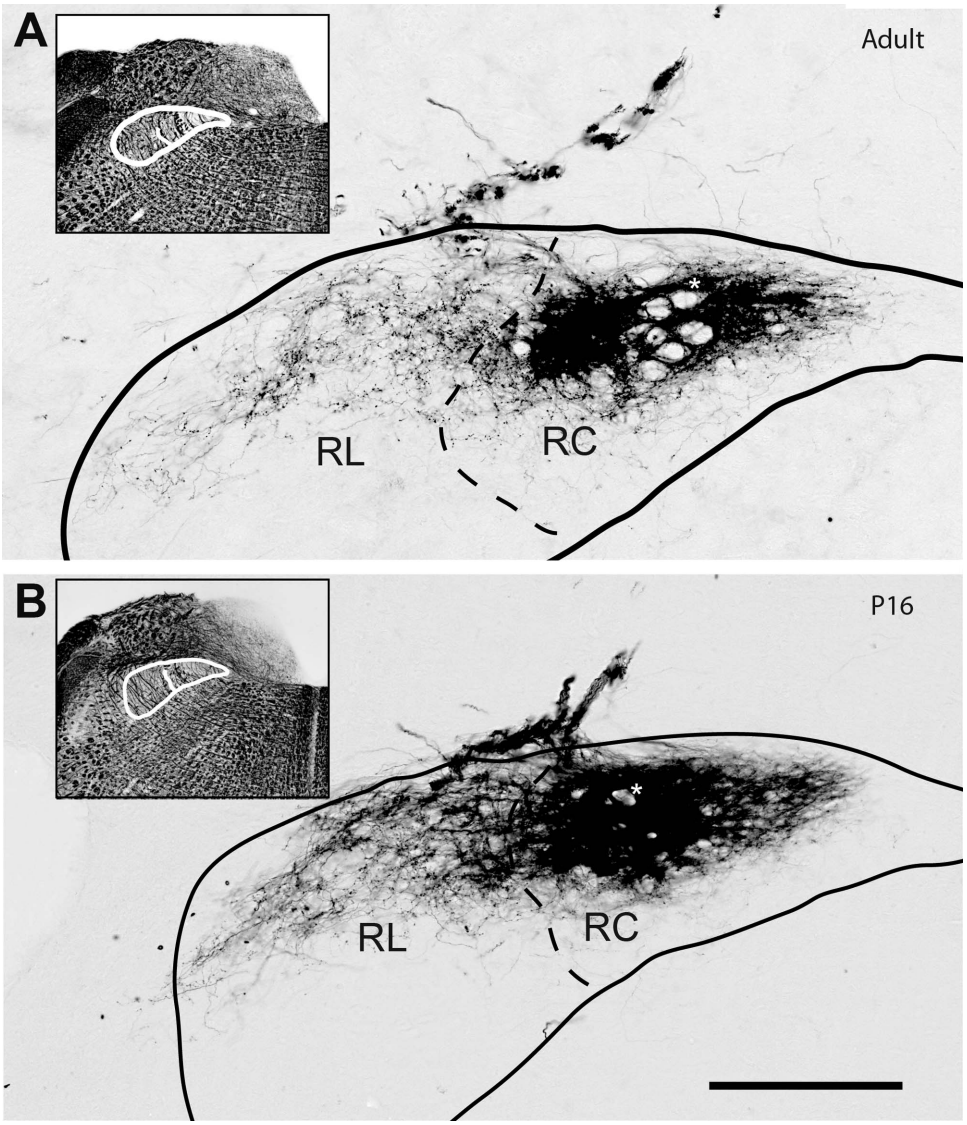

Figure 2. The distribution of CT terminal field in the rostral portions of the NTS at adulthood (**A**) compared with p16 (**B**). Both sections were located about 450 μm posterior to the rostral pole of the NTS. The subdivision borders are identified on adjacent Nissl- and myelin-stained (insets in both panels display myelin-stained sections with outlines) sections and superposed on the anterograde DAB-labeled sections. The spread of CT labeling in the p16 animal is very similar to that of the adult. In both ages the densest terminal field is found in the rostrocentral (RC) while sparser labeling in the rostrolateral subdivision (RL) covers the dorsal half and extends to the lateral NTS border. However, the qualitative density of the fiber populations is quite different. The terminal field in the rostrolateral subdivision is much denser at p16 than in the adult. At this level the solitary tract appears as sparse yet thick bundles of axons coursing anterior to posterior direction through the labeled fields in rostrocentral subdivision (marked with an asterisk). Scale bar = 250 μm.

seemed similar between two ages (Fig. 1A–C vs. D–F). However, the anteroposterior dimensions of NTS were considerably smaller in P15 brains: The mean distance from the area postrema landmark (AP = 0, the most anterior coronal section in which area postrema was present) to the rostral pole was 2.36 ± 0.08 mm in adult ($n = 3$) and 1.95 ± 0.04 in P15 ($n = 5$) animals ($P < 0.02$, t-test).

In adult brains, three distinct zones of CT axonal projections were evident (Figs. 2A, 3A, 4A) in the rostrocentral, rostrolateral, and ventrolateral subdivisions. In the rostrocentral subdivision, labeled CT axons formed a dense plexus of fibers (Fig. 2A), and was qualitatively distinct from less densely packed and thick fibers of rostrolateral (Fig. 2A) and ventrolateral subdivisions (Figs. 3–4A) of the NTS. The transition between the rostrocentral and rostrolateral projections was not gradual; a clear separation of distinct anatomical structures was often evident (Figs. 2–3A). A dense CT-projection region remained within the confines of the rostrocentral subdivision borders. At approximately the coronal level that NTS

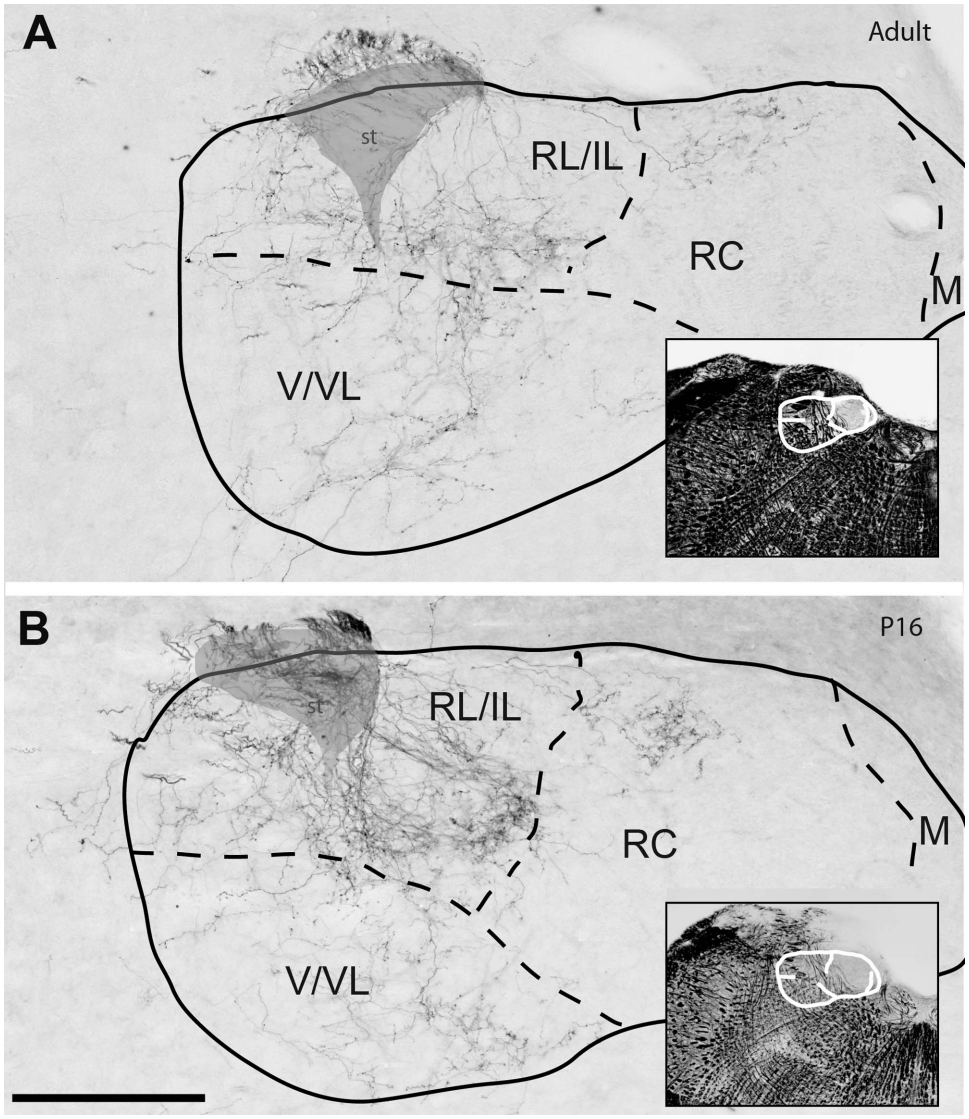

Figure 3. The distribution of CT terminal field in the intermediate portions of the NTS at adulthood (**A**) compared with p16 (**B**). The subdivision borders (dashed lines) and an envelope of solitary tract (shaded gray) are identified on adjacent Nissl- and myelin-stained (insets in both panels) sections and superposed on the anterograde DAB-labeled sections. Both sections were located just anterior to the NTS-fourth ventricle junction, the operatively defined transition region between rostrocentral subdivision and caudal NTS, and between ventral and ventrolateral subdivisions (V/VL). CT axons are present sparsely in all compartments. As with rostral sections, terminal field labeling appears qualitatively denser in the p16 than the adult NTS, while subdivisional distribution of label in the NTS appears the same. The intermediate-lateral (IL) subdivision, which is defined by lack of CT innervation in adult brains, is also devoid of fibers at P16. Scale bar = 250 μm.

separates from the fourth ventricle (operationally defined as the border between rostral and caudal divisions of NTS), sparse CT fibers surrounded and avoided a distinct region, which we previously identified as the intermediate lateral subdivision (Corson et al., 2012). The sparse CT projections are detected throughout the NTS, from the rostral pole to as caudal as 600 μm posterior to the AP landmark. It should be noted that the densely labeled rostrocentral subdivision of the NTS was the focus in our previously published material (May et al., 2007, 2008).

Similar to the adult, P15 CT axons appeared in three distinct zones in the NTS; densely branching fine fibers were confined to rostrocentral subdivision and sparsely branching thick fibers spread in rostrolateral and ventrolateral subdivisions (Figs. 2B, 3B, 4B). The shape and qualitative density of CT fibers in the rostrocentral subdivision in P15 was similar to that in adult. Similar to adult brains, there were sparsely branching, thick CT axons in regions lateral, and ventral to rostrocentral subdivision. However, the

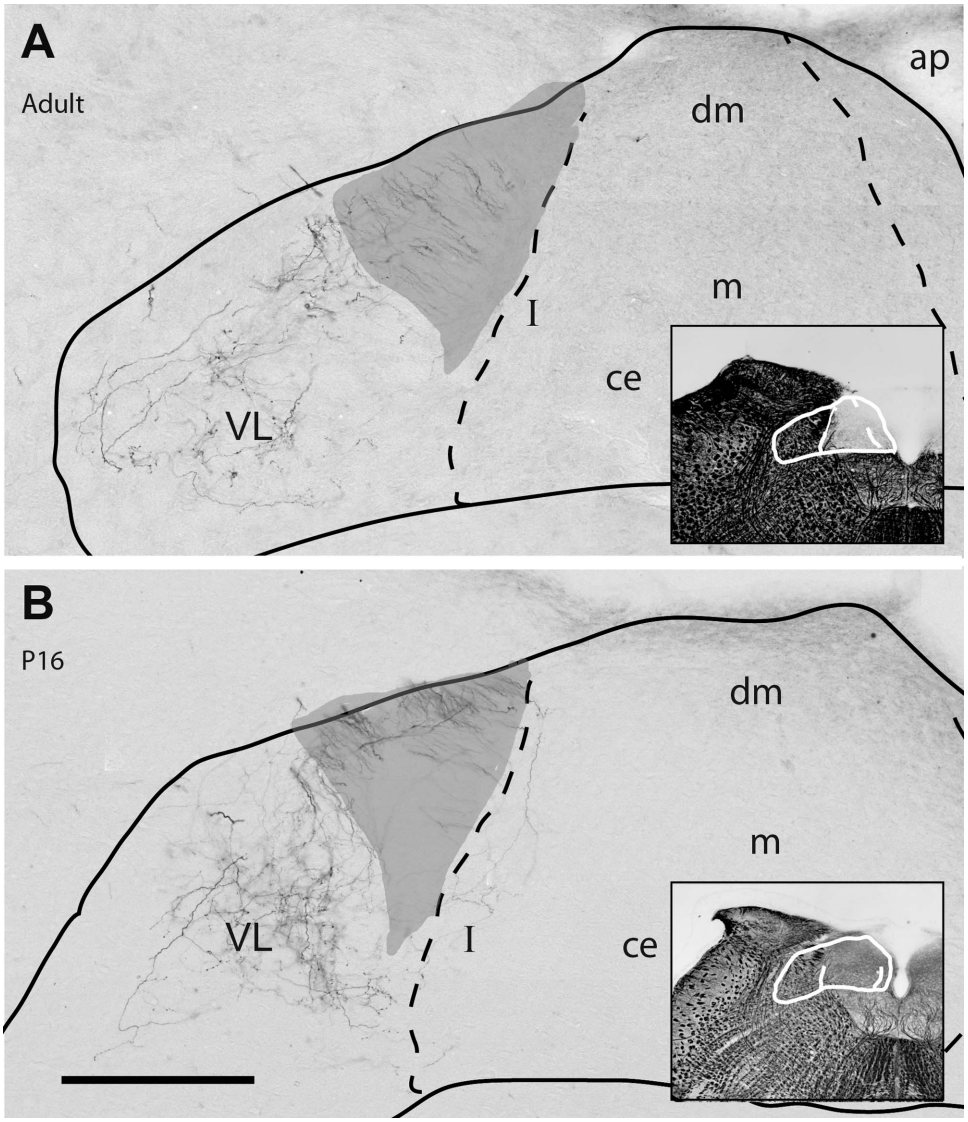

Figure 4. The distribution of CT terminal field in the caudal portions of the NTS at adulthood (**A**) compared with p16 (**B**). The subdivision borders (dashed lines) are identified on adjacent Nissl and myelin sections and were superposed on the anterograde DAB-labeled sections. Both sections were located at levels where the NTS borders the anteriormost portion of area postrema (i.e., AP = 0). Sparse terminal field is found only in the ventrolateral subdivision (VL). Labeled fibers, which do not bear any swellings (i.e., axons of passage), course through the solitary tract (shaded gray). Subnuclei in caudal NTS are identified based on terminology and criteria defined in Herbert et al. (1990). As with rostral and intermediate sections, terminal field labeling appears qualitatively denser in the p16 and adult animal, while distribution pattern of label in NTS subdivisions is similar. ce, central nucleus; pc, parvicellular nucleus; m, medial nucleus; dm, dorsomedial nucleus; I, intermediate nucleus; ap, area postrema. Scale bar = 250 μm.

qualitative density of these axons was visibly more pronounced in P15 than in the adult (Fig. 3B). The intermediate lateral subdivision, which receives afferent inputs from IX nerve but not from CT or GSP in adult animals (Corson et al., 2012), was devoid of CT fibers, both in adult and P15 brains (Fig. 3). These patterns of CT afferent innervation in P15 and adult brains suggest that exuberant projections found in P15 animals do not extend beyond the NTS subdivisions that they will eventually occupy at adulthood.

In order to quantitatively evaluate the extent of axon withdrawal from NTS subdivisions between P15 and adult ages, the entire NTS was examined in five P15 and three adult animals (Fig. 5), noting the distance of posterior and anterior borders of CT labeled regions in rostrocentral, rostrolateral, and ventrolateral subdivisions relative to the AP landmark (AP = 0). The anterior–posterior distance between the rostral pole of the NTS and AP = 0, and between where the NTS contacted the fourth ventricle and AP = 0 were also noted. As conventional in the

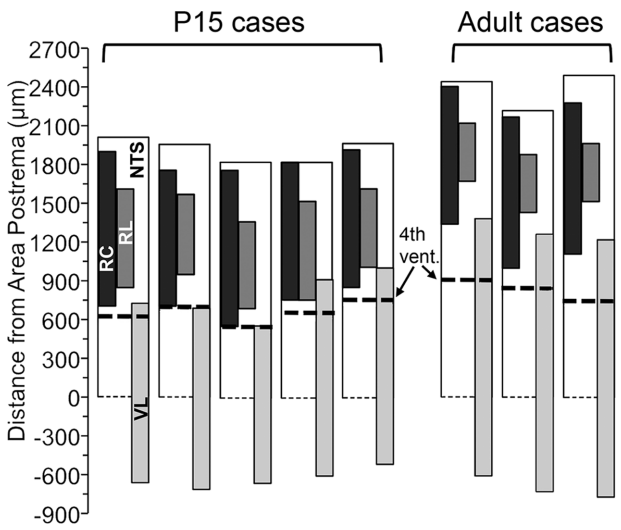

Figure 5. Illustration of anterior–posterior size of NTS and CT labeling by subdivision from the rostral pole to area postrema landmark (AP0; the anteriormost coronal section that AP is present) in each of five P15 and three adult animals. The anteriormost section that NTS lined the fourth ventricle marked with dashed lines for each brain; this landmark is conventionally designated the arbitrary border of rostral and caudal NTS. Open bars indicate the expanse of NTS from AP0 to the rostral pole. Filled bars superposed on open bars illustrate the expanse of CT labeling found in NTS subdivisions identified in adjacent Nissl/myelin reference sections. Black bar denotes CT label in the rostrocentral subdivision, dark gray bar in the rostrolateral subdivision, and light gray bar in the ventrolateral subdivisions. Because the caudal pole of NTS could not be identified in our material, the extension of NTS posterior to AP0 is not illustrated; however, all sections that displayed CT label in ventrolateral subdivisions are included. The NTS in all adult brains was significantly larger than in P15 brains. While CT label in rostrocentral subdivision did not differ between p15 and adult, more sections contained CT terminal field in the rostrolateral subdivision in P15 than in adult.

past literature, this landmark is used as the arbitrary border of rostral and caudal divisions of NTS. While the AP0 to rostral pole distance is larger in the adult (1,900 ± 41 μm in P15 vs. 2,316 ± 78 μm in adult, $P = 0.01$, reported above), fourth ventricle to rostral pole size was not statistically different (1,240 ± 33 in P15 vs. 1,483 ± 108 μm in adult, $P = 0.14$). However, interestingly for every case, the rostrocentral labeling was closer to the NTS-fourth ventricle junction in P15 than in adult ($P < 0.05$, *t*-test; Fig. 5). Thus, the growth of NTS size between P15 and adult occurs mainly in the caudal divisions of the NTS.

Examination of CT labeling in the anterior–posterior axis revealed that while CT projections (i.e., number of coronal sections containing CT label) in the rostrocentral subdivision did not differ between P15 and adult (1,080 ± 56 μm vs. 1,050 ± 0 μm; $P = 0.6$, *t*-test), the CT input in the rostrolateral subdivision was significantly larger in P15 than in the adult (690 ± 36 vs. 450 ± 0 μm; $P = 0.003$, *t*-test; Fig. 5A). In contrast, ventrolateral projections occupied a larger area in the adult (1,380 ± 56 μm in P15 vs. 1,950 μm in adult, $P < 0.001$, *t*-test). These results suggest that CT axon retraction after P15 occurs mainly in the rostrolateral subdivision. In contrast, CT axons continue to expand caudally in the ventrolateral subdivisions after P15, possibly paralleling the anterior–posterior growth of NTS.

Electron microscopic characterization of CT projections

Morphology of rostrocentral CT terminals

In order to quantify morphological maturation of CT axons from P15 to adulthood, regions from the middle of dense CT projections medial to solitary tract (which coincides with the center of rostrocentral projection field) were examined with the electron microscope. As described previously by May et al. (2007), CT terminals appeared as densely DAB-labeled profiles, with dark mitochondria and clear vesicles, forming asymmetric synapses onto dendrites with varying calibers (Fig. 6). The synapses formed by CT terminals displayed thick postsynaptic densities and occasional perforations (Fig. 6C). Protrusions emerging from postsynaptic profiles that extended into the terminal bouton were also observed (Fig. 6C). Although unbundled myelinated axons coursed through the CT projection field in the rostrocentral subdivision (Fig. 6E,F), none of these myelinated axons contained the DAB label, suggesting that CT axons that extend to terminate in the rostrocentral subdivision are unmyelinated. There were no qualitative differences in label quality, labeled terminal morphology, or neuropil packing among brains at any age examined (Fig. 6A–F).

For quantitative analysis, minimally overlapping regions labeled terminals that displayed a synapse at the level of section were imaged in three brains each at P15, P25, P35, and adult. Comparisons of quantitative morphometric properties of rostrocentral terminal boutons revealed that CT terminals attain morphological properties characteristic of adult animals before P15, the youngest age examined. This was evident in several parameters examined: Although a wide range of terminal cross-section areas were found at all ages (0.12–5.0 μm^2), no statistical difference of terminal cross-section area means or distributions was found between any consecutive age group studied (mean terminal cross-section areas were 1.26 ± 0.10 μm^2 ($n = 73$) in P15, 1.28 ± 0.12 μm^2 ($n = 62$) in P25, 1.36 ± 0.11 μm^2 ($n = 59$) in P35, and 1.29 ± 0.12 μm^2 ($n = 55$) in adult animals; $P > 0.5$; Kruskal–Wallis and Mann–Whitney *U*; Table 1, Row A). Terminal cross-section areas obtained from adult animals were statistically comparable to previously published

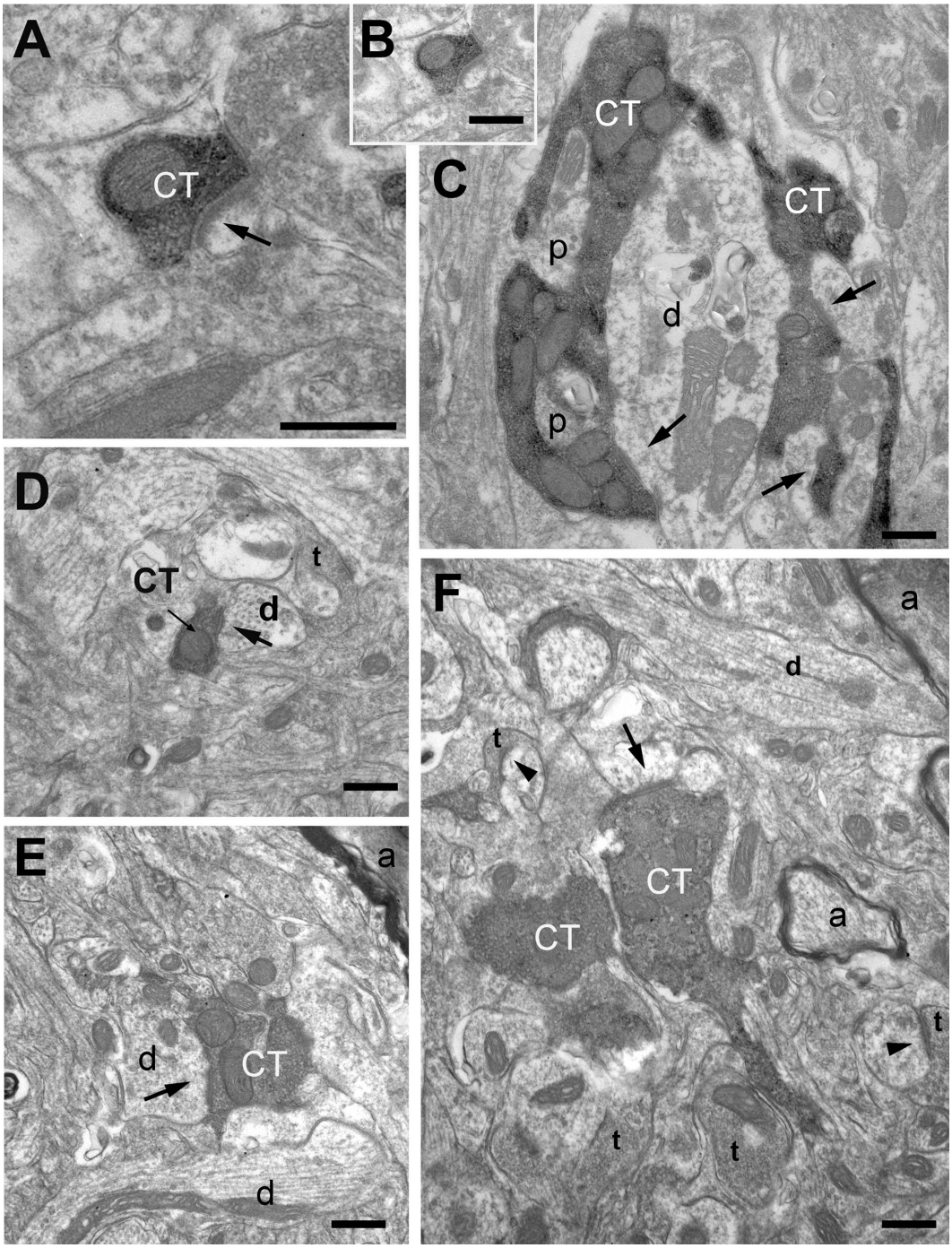

Figure 6. Electron microscope images of CT terminals from rostrocentral NTS, in adult **(A–C)**, and P15 **(D–F)** brains. Qualitatively and quantitatively, CT terminals in P15 are indistinguishable from those in adult. A: High-magnification view of a small CT labeled terminal forming a synapse with thick postsynaptic density. At both ages, terminals with a wide range of cross-section areas, including small en passant terminals (B,D) and large terminal boutons (C,E,F), which may contain unlabeled inclusions (p) protruding from postsynaptic dendrites (d). Arrows point to asymmetric synapses formed by labeled CT terminals (CT); arrowheads point to other sample synapses within the same field formed by unlabeled terminals (t). Myelinated axons (a) were encountered within the same region; no instances of label containing myelinated axon was encountered in rostrocentral NTS Scale bars = 0.5 μm.

measurements (May et al., 2007). Similarly, we measured the length of synaptic zones of labeled CT terminals, an index for the diameter of active zones. These also displayed a wide range of cross-sectional lengths (compare synapses in Fig. 6B,D to 6C,F), and there were no statistical differences among the means or the distributions at different ages (359 ± 18 nm (n = 88) in P15, 354 ± 19 nm (n = 73) in P25, 363 ± 18 nm (n = 63) in

TABLE 1.

Quantitative Parameters for Chorda Tympani Axon and Terminal Development in the NTS

	P15	P25	P35	Adult
A: Terminal area –rostrocentral (μm^2)	1.26 ± 0.1 ($n = 73$, b)	1.28 ± 0.1 ($n = 62$)	1.36 ± 0.1 ($n = 59$)	1.29 ± 0.1 ($n = 55$, a)
B: Terminal area –rostrolateral (μm^2)	1.46 ± 0.1 ($n = 181$, b)			1.42 ± 0.1 ($n = 100$, a)
C: CT axon density rostrocentral (μm axon/μm^2)	0.15 ± 0.01	0.19 ± 0.01	0.19 ± 0.04	0.16 ± 0.01
D: Synapse count per mm axon (synapsing frequency)	162.8 ± 8.4 (c, d, e)	111.1 ± 7.5 (c,f)	102.7 ± 14.4 (d, g)	70.3 ± 2.6 (e, f, g)
E: Volumetric Density of CT terminals ($X10^6$ synapses/mm^3)	66 ± 2 (h)	62 ± 3	58 ± 3 (h, i)	34 ± 9 (i)
F: Volumetric density of all synapses in rostrocentral ($X10^6$ synapses/mm^3)	282 ± 33	252 ± 15	233 ± 15	211 ± 29
H: Percent GABA+ targets of CT terminals	9.1% ± 0.3 (j, k, l)	5.1% ± 0.4, (j)	4.5% ± 0.7 (k)	3.5% ± 0.5 (l, m)
I: Percent of GABA+ targets of all rostrocentral terminals	9.4% ± 2.3	6.4% ± 1.8	6.5% ± 1.2	7.8% ± 0.8 (m)

Averages are based on three brains at each age group, unless specified otherwise for pooled observations for terminal cross-section area analysis. The statistical comparisons that yielded significant differences are marked with matching letters in parentheses. $P < 0.05$ (a,b, f, g, k, l, m); $P < 0.005$ (c, d, e, h, i, j).

P35, 400 ± 22nm ($n = 63$) in adult; $P = 0.4$). About 12% of individual terminal cross-sections formed two synapses onto two separate cross-sections (this is also why terminal area and synapse length measurements that were obtained from the same image dataset yielded different sample sizes). The lack of growth in terminal bouton and active zone sizes suggests that major morphological development of CT axon boutons in rostrocentral subdivision is complete by P15.

Morphology of rostrolateral CT terminals

Similar to those in the rostrocentral subdivision, axon segments and vesicle-containing boutons were labeled in the rostrolateral subdivision. Several differences between CT terminals in the rostrocentral and rostrolateral subdivisions were noted. First, we observed that instances that CT terminals were located within glomerular arrangements were more frequent in the rostrolateral subdivision (Fig. 7A). Glomerular arrangements are identified as collections of several terminals and dendrites that are ensheathed with glial processes only from their collective external aspect. In order to quantify the involvement of CT terminals within, we examined labeled terminals in rostrocentral and rostrolateral subdivisions from the same brain. Applying the criteria for glomerulus designation that 1) a labeled terminal shared membrane apposition with at least two other profiles, and 2) at least two of the profiles were surrounded by glial processes, we found 24% in rostrolateral versus 8% in rostrocentral CT terminals could be identified as glomerular ($n = 60$ and 48). Second, the occurrences that labeled terminals formed synapses onto unlabeled, vesicle containing profiles were more common in the rostrolateral regions (Fig. 7C). Such axo-axonal synapses, commonly wrapped by glial processes, were not commonly encountered in the rostrocentral subdivision. Finally, in the rostrolateral subdivision we frequently encountered myelinated DAB-labeled axons (Fig. 7B). In all rostrocentral sections examined, no instances of labeled myelinated axons were observed, indicating that rostrolateral, but not rostrocentral, CT axons are myelinated.

Rostrolateral terminal cross-section areas

In the rostrolateral division of adult brains, CT terminals had a mean terminal cross-section area of 1.42 ± 0.09 μm^2 ($n = 100$; Table 1, Row B), and this was statistically larger than for terminals in the rostrocentral region (1.29 ± 0.12 μm^2; $n = 55$; Mann–Whitney U, $P < 0.05$). We repeated this experiment using material prepared for a previously published study (May et al., 2007), and again found rostrolateral terminals to be statistically larger than the rostrocentral terminals (1.41 μm^2 vs. 1.24 μm^2; $n = 38$ and 81, Mann–Whitney U, $P < 0.05$). Figure 7D illustrates pooled data from these two experiments. Furthermore, the size difference between rostrolateral and rostrocentral terminals was also evident in P15 brains (Fig. 7E; Table 1, Row B). At P15, rostrolateral terminals had an average cross-sectional area of 1.46 ± 0.08 μm^2 ($n = 181$), which was statistically larger than in the rostrocentral (1.26 ± 0.1 μm^2; $n = 73$; Mann–Whitney U; $P < 0.05$). Rostrocentral and rostrolateral terminals found in P15 were not statistically different than their adult counterparts (Fig. 7F,G). Thus, CT terminals in the rostrolateral subdivision are morphologically distinct from those in the rostrocentral projection region. Furthermore, similar to in rostrocentral, CT boutons in rostrolateral subdivision display mature-like (i.e., terminal cross-section area and synapse length) morphological features at P15.

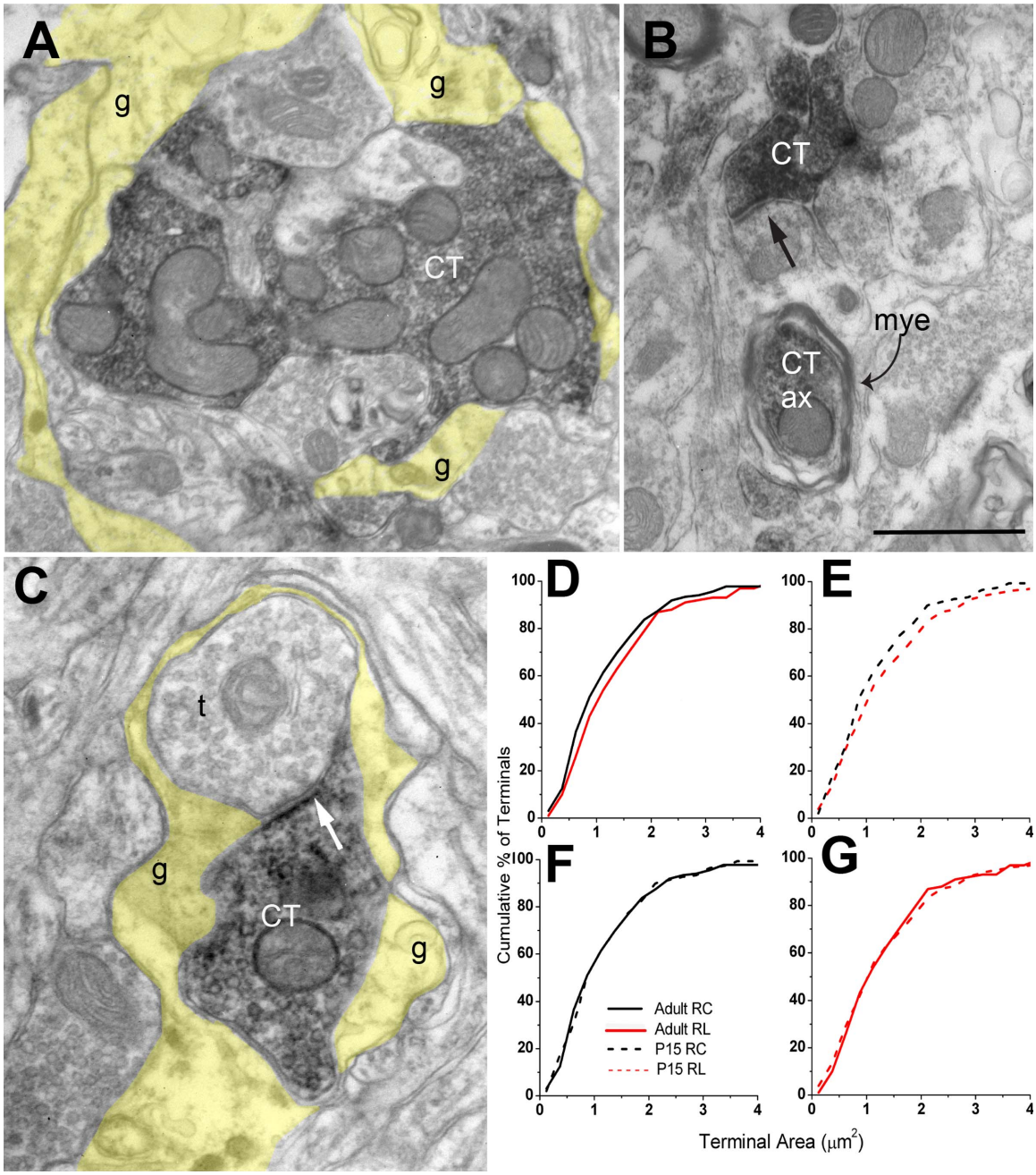

Figure 7. **A:** A large rostrolateral CT terminal (CT) is located in a glomerulus, ensheathed in glial processes (tinted yellow). This glomerulus also contains other dendrites and axons, which are unlabeled. **B:** Rostrolateral CT terminal field often contained labeled myelinated (mye) axon segments (Ct ax). **C:** A labeled CT axon forms a synaptic contact with another vesicle filled profile (t); these two profiles are ensheathed with glial processes (tinted yellow), suggesting that the synapse is part of a glomerulus. Images in A–C were obtained within rostrolateral subdivision of an adult brain. **D–G:** Terminal cross-section area comparisons of CT terminal populations sampled in rostrocentral subdivision (RC) in the adult (black solid line), in rostrolateral subdivision (RL) in the adult (red solid line), rostrocentral subdivision in P15 (black dashed line), and rostrolateral subdivision in P15 (red dashed line). Pairs in D,E were statistically different from each other. Scale bar in B represents 390 nm for A, 450 nm for B, and 300nm for C.

CT branch reduction in NTS subdivisions

Previous work indicated that the CT terminal fields in the NTS go through an extensive "pruning" during maturation (King and Hill, 1991; Krimm and Hill, 1997; May and Hill, 2006; Sollars et al., 2006; Mangold and Hill, 2007, 2008). In these studies, the "pruning" is inferred from the reduction of the NTS volume occupied by labeled afferent axons, which conceivably included rostrocentral and rostrolateral projections. In agreement with those findings, the material prepared in this study revealed a reduction

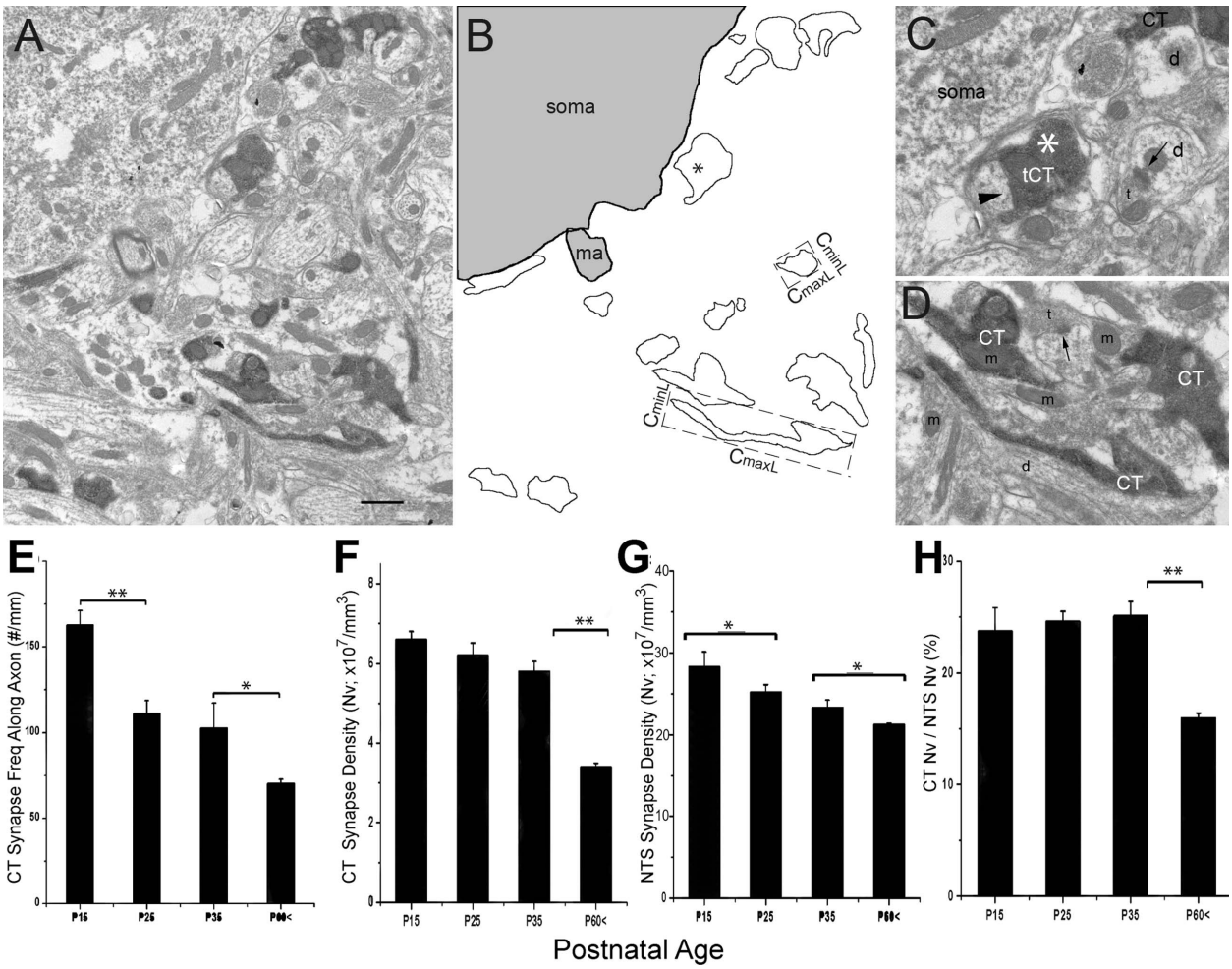

Figure 8. **A,B:** Method for quantifying CT axon areal density. A: Low-magnification electron micrograph example of CT terminal field. B: To calculate total area of neuropil analyzed, the image area was measured, excluding the areas of somata (soma) and myelinated axons (ma; excluded areas are shaded gray). All labeled profiles are outlined, and the ones that form a synapse (*, also in C) are identified. All outlines are used in computation of Cmax and Cmin (feret-max and feret-min functions of Image ProPlus; dashed lines at two representative outline). **C:** High-magnification view of the synapse-forming terminal from A (tCT). Arrowhead points to the CT synapse. Arrows point to synapses from unlabeled terminals. **D:** High magnification of representative cross-section of CT fibers (CT) that do not bear a synapse at the current level of section. Unlabeled vesicle containing profiles (t) in proximity are marked for comparison. d, dendrite; m, mitochondria. **E:** The frequency of synapses formed along the CT axon (number of synapses/total length of labeled fiber observed). **F:** Volumetric synapse density of the CT terminals. **G:** Volumetric synapse density of all synapses in the same region. **H:** Percent ratio of CT volumetric density to total volumetric density in the rostrocentral subdivision. Error bars indicate the standard error of mean; $*P < 0.05$, $**P < 0.01$. Scale bar = 1 μm. Panels C and D are 1.5X enlargements from Panel A.

of NTS area that was occupied by CT axons between P15 and adult ages (Figs. 1–5). Furthermore, identification of NTS subdivision borders in adjacent myelin and Nissl coronal series revealed that the most substantial reduction in the NTS volume occupied by CT axons occurred from rostrolateral subdivision (Fig. 5); a similar reduction was not observed in rostrocentral subdivision. In order to further explore the possibility that CT axon retraction may have impacted rostrocentral subdivision innervation via elimination of branches within the confines of this region, a quantification of labeled fiber density was required. Fiber density measurements in rostrocentral CT using light microscopy were not feasible in our material due to the density of the plexus of CT axonal branches. We took advantage of a quantification approach we previously optimized (Erisir and Dreusicke, 2005; May et al., 2007). This approach uses ultrathin sections and estimates the length of axon represented by each axon cross-section (Fig. 8A–D). Comparisons of areal CT axon densities across the developmental ages revealed no significant differences ($n = 3$ at each age, $P > 0.15$, Table 1, Row C), suggesting that CT axon branches are not pruned back within the rostrocentral subdivision of the NTS during development.

Development of rostrocentral circuitry.

While qualitative observations indicate that CT axons become unambiguously sparser in the rostrolateral NTS between P15 and adult, more subtle changes occur in the rostrocentral subdivision circuitry. Even though no change in the density of CT axons in rostrocentral subdivision was detected, the number of synapses per unit length of labeled axons (computed as "synapsing frequency of labeled axons") changed (Fig. 8E). Progressively fewer synapses were formed per unit length of axon as the animal aged from P15 to adult. At P15 there were significantly more synapses per millimeter of axon than at the other three age groups (Table 1, Row D; 162.8 $\pm$ 8 synapses/mm of axon at P15; 111.1 $\pm$ 7 synapses/mm at P25; 102.7 $\pm$ 14 synapses/mm at P35; and 70.3 $\pm$ 2 synapses/mm of axon at adult; $P < 0.005$). Adults also had significantly fewer synapses per axon length than P25 and P35 rats ($P < 0.05$).

Synaptic pruning without axonal retraction in the rostrocentral region after P35 was also evident in the volumetric density of CT synapses (Fig. 8F; Table 1, Row E). In three brains at each age, over 1,000 μm^2 (per brain) of tissue was examined and volumetric densities of labeled synapses were computed. There was a significant reduction in CT synapse density in NTS, most prevalently between P15 and P35 ($P < 0.05$) and between P35 and adult ($P < 0.001$, ANOVA; volumetric density of CT synapses were 66 $\pm$ 2 $\times$ 10^6 synapses/mm^3 at P15; 62 $\pm$ 3 $\times$ 10^6 at P25; 58 $\pm$ 3 $\times$ 10^6 at P35, and 34 $\times$ 10^6 $\pm$ 9 at the adult).

Reduction in CT synapse density may simply be due to an increase in NTS neuropil volume (perhaps via expansion of dendrites or increase in astrocytic volume), without necessarily having an impact on the CT circuitry. If that is the case, increases in neuropil volume should also reduce the density of all synapses in the region. In order to determine whether the rostral NTS undergoes a general synapse reduction, the volumetric density of all synapses within the same the images used for CT terminal volumetric density was measured (Fig. 8G). Overall synapse density in NTS displayed a statistically significant trend toward reduction between P15 and adult (282 $\pm$ 31 $\times$ 10^6 synapses/mm^3 at P15; 252 $\pm$ 15 $\times$ 10^6 at P25; 233 $\pm$ 15 $\times$ 10^6 at P35 and 211 $\pm$ 29 $\times$ 10^6 at the adult; $n = 3$ for each age, average $\pm$ SEM; ANOVA, $P < 0.05$; Table 1, Row E), suggesting that neuropil expansion may have occurred. However, the pattern of reduction in CT synapse volumetric density was not proportional with the volumetric density of all synapses (Fig. 8F,G); the contribution of CT synapses to overall rostrocentral synapse density drops from 25.1% to 16.0% between P35 and P60. This reduction in ratios of CT versus all rostrocentral synapses was statistically significant (ANOVA, $P < 0.01$; Fig. 8H), suggesting that in addition to neuropil enlargement, selective loss of CT synapses may have contributed to their reduction from rostrocentral circuitry.

The targets of CT axons in the NTS include inhibitory interneurons, which can be identified by their GABA content. In order to identify how CT synapse elimination in NTS may reflect on particular postsynaptic targets, selectivity of CT synapses for GABA+ and GABA− targets during development was analyzed. For this, NTS sections containing CT labeled terminals were immunogold-stained using an antibody against GABA and postembedding procedures. While antibodies against glutamic acid decarboxilase are better markers for GABAergic cell dendrites at the light microscopy level (Fong et al., 2005), GABA-immunogold electron microscopy has been successfully used in quantitative analysis of GABAergic neuropil in a variety of systems. In order to quantify the frequency that a CT synapse was formed onto GABAergic versus non-GABAergic dendrites, P15, P25, P35, and the adult brains were dually stained for the tracer marking CT axons (preembedding), and for GABA (postembedding; Fig. 9). It should be noted that while the area of interest for this analysis was again the center of rostrocentral subdivisions, due to compromise of tissue landmarks during postembedding processing, conceivably a small number of terminals from rostrolateral subdivision may have been included in the sample. Three brains at each age were examined, and the percentages obtained at each age were averaged. Background gold density was assessed within terminals that remained unlabeled with DAB; most of these terminals displayed clear asymmetric synapse morphology (presumed glutamatergic), although a range of postsynaptic density thickness was present. Terminals that displayed unambiguously symmetrical (presumed GABAergic) morphology were excluded from background criterion measurements. Gold density at the 95th percentile confidence level was applied as the criterion to classify dendrites postsynaptic to DAB-labeled terminals. Criterion density obtained for each ultrathin section examined yielded a clear separation of postsynaptic dendrites into GABAergic and non-GABAergic populations (Fig. 9A). The same criterion also provided a clear separation of GABA immunoreactivity within general dendrite populations in the same sections (Fig. 9A), confirming the reliability of the background criterion. Reliability of the background criterion was also tested within morphologically identified, symmetrical (presumed GABAergic) terminals in P15 ($n = 20$ terminals) and adult ($n = 20$ terminals) brains; none of the terminals with symmetrical synapse morphology in P15 and adult brains had GABA-gold density smaller than the 99th percentile criterion. In order to quantify the preference of CT terminals for GABAergic targets, at least 100 DAB labeled synaptic

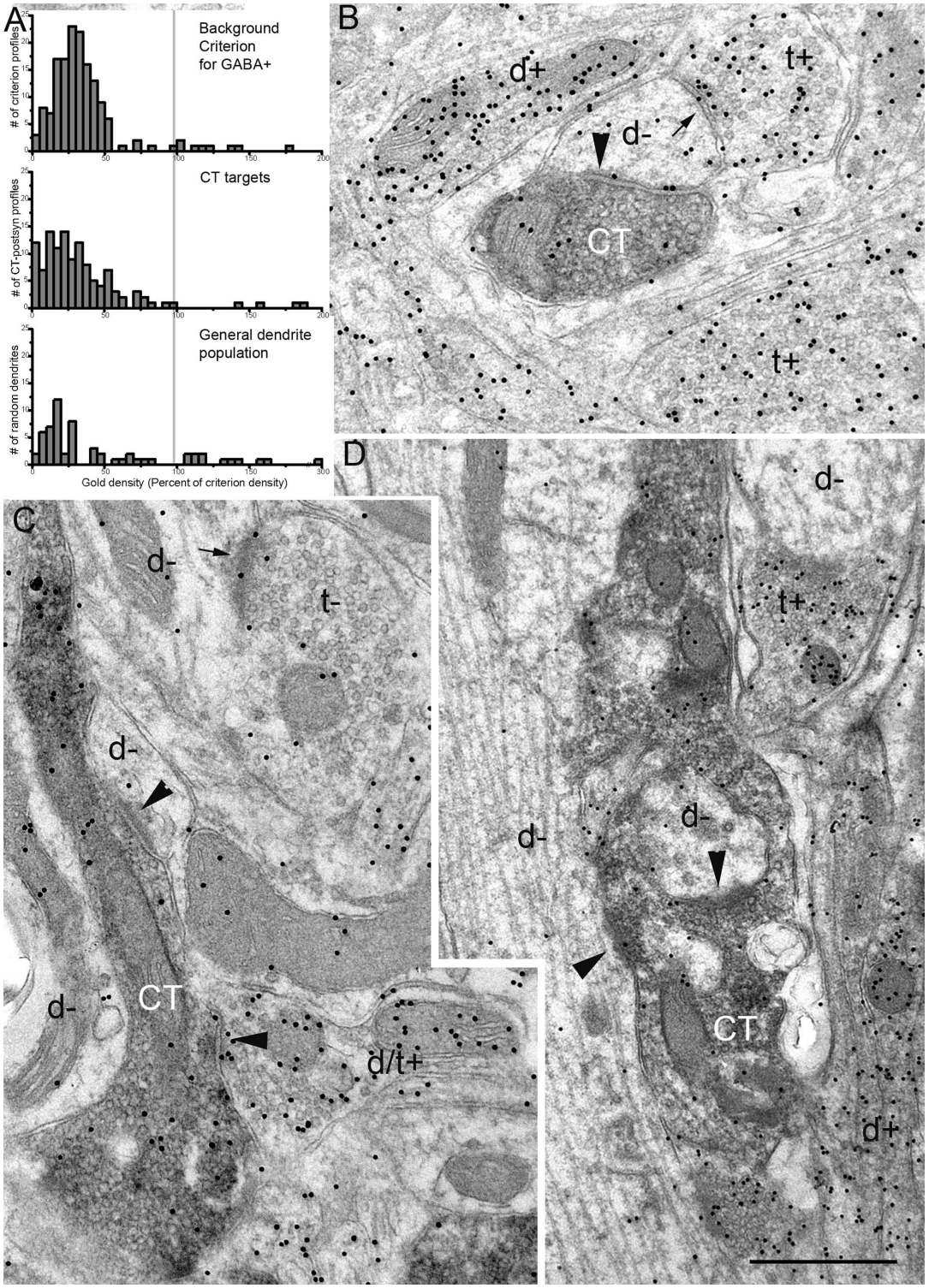

Figure 9. **A:** Top panel: Frequency distribution of gold densities measured in DAB-negative terminals displaying asymmetric synapses in a representative brain. The 95th percentile value was deemed the criterion gold density for GABA positivity, and applied to the gold densities measured in profiles postsynaptic to CT labeled terminals (middle panel). The criterion gold density (vertical gray line) also divided a general dendrite population measured within the same section (bottom panel) as GABA+ and GABA− groups. **B:** A CT terminal (CT) from an adult brain forms an asymmetric synapse (large arrowhead) onto a GABA− dendrite (d−). Compare the gold density within the postsynaptic dendrite with that in surrounding terminals (t+; thin arrow points to a symmetrical synapse in one) and a dendrite (d+), which contained above-criterion gold density. **C:** A CT terminal forms two synapses (arrowheads): one onto a GABA− dendrite (d−) and another onto a GABA+ profile that contained vesicles (d/t+). **D:** A CT terminal at P15, bearing unlabeled inclusions, forms two synapses (arrowheads) onto a large caliber GABA− dendrite, and a GABA− inclusion. A GABA+ terminal (t+) and a GABA+ dendrite (d+) are also present in the same field. Scale bar = 0.5 μm; applies to all panels.

terminals each from three brains for each age were examined (total from three brains at each age: 329, 332, 384, and 340, in P15, P25, P35, and adult brains, respectively). The P15 rats had a significantly higher percentage of CT synapses onto GABAergic targets than in other three age groups, displaying a significant drop between P15 and P25 (9.1 $\pm$ 0.3% vs. 5.1 $\pm$ 0.4%; $n = 3$ at each age, *t*-test, $P < 0.005$), and a further decline between P35 and the adult (4.5 $\pm$ 0.7% vs. 3.5 $\pm$ 0.5%, $n = 3$, $P < 0.005$). Interestingly, many of GABA+ targets of CT terminals at all ages also contained vesicles (Fig. 9C). These postsynaptic GABA+, vesicle-filled profiles probably represent dendritic appendages that are known to contribute to triadic arrangements in the NTS glomeruli (Whitehead, 1986). Furthermore, all CT targets that contained vesicles were GABA+.

Because GABA antigenicity in developmental animals may differ irrespective of the changes in GABA-containing neurons, it is important to assess whether reduction of GABA-positive dendrites that are postsynaptic to CT terminals is a function of a general shortcoming of immunocytochemistry in older animals. To that end, we assessed whether non-CT synapses were subject to a similar redistribution as CT synapses: Non-CT synapses (389 in P15, 381 in P25, 428 in P35, and 394 in adult brains, total in three brains each) and their postsynaptic targets were examined in the same sections from which CT-GABA analysis were performed. The ratio of non-CT terminals that synapsed on a GABAergic target did not change across ages examined (9.4 $\pm$ 2.3% in P15, 6.4 $\pm$ 1.8% in P25, 6.5 $\pm$ 1.2% in P35, and 7.8 $\pm$ 0.8% in adult, $P > 0.1$), suggesting that the observed reduction of CT-GABA connections was not an outcome of a general reduction in GABAergic targets or the antibody antigenicity in the rostrocentral NTS during developmental ages.

DISCUSSION

The results of this study demonstrate that: 1) CT axons occupying the rostrolateral subdivision of NTS both in the adult and P15 rats are morphologically distinct from CT axons that innervate the rostrocentral, gustatory subdivision of the NTS; 2) CT terminals reach morphological maturity before P15 in both the rostrocentral and rostrolateral subdivisions; 3) rostrocentral CT projections are spared from substantial axonal branch elimination that is qualitatively observed in rostrolateral NTS after P15; 4) CT synapses become a smaller component of the total synaptic inputs to the rostrocentral NTS after P35; and 5) the preference of CT synapses for GABAergic targets drastically falls between P15 and P25, indicating a redistribution of CT synapses onto NTS targets.

Morphological and functional heterogeneity of CT projections in rostrocentral vs. rostrolateral NTS

Past studies suggested that the CT may bring at least two morphologically distinct inputs into the NTS (Holland and Robinson, 1992), based on the presence of at least two subpopulations of afferent CT axons with different calibers and myelination properties (Farbman and Hellekant, 1978). This morphological heterogeneity may be reflected by the functional heterogeneity in the CT. Gustatory, mechanical, and thermal stimulation of the tongue all generate responses in the CT (Nejad, 1986; Harada et al., 1997). While it is likely that temperature responses may be partially due to dynamic changes in a subset of taste receptors, rather than activating a specialized thermoreceptor (Ogawa et al., 1968; Ninomiya, 1996; Lundy and Contreras, 1999), at least a subset of CT fibers responds exclusively to mechanical stimulation, and others respond exclusively to taste or to a combination of taste and mechanical stimulation (Biedenbach and Chan, 1971; Matsuo et al., 1995; Smith et al., 2004). Similarly, iatrogenic damage to the CT leads to taste loss, as well as numbness, tingling, and pain (Costen et al., 1951; Perez et al., 2006). Such a loss of complex neural information is consistent with the idea that this nerve conveys multimodal orosensory information in addition to taste, and that functionally distinct subsets of the CT selectively innervate different subdivisions in the NTS.

Axonal and synapse elimination and reorganization after P15

Previous light microscopic studies clearly showed a compaction of the CT projection zone between P15 and adulthood (May and Hill, 2006; Sollars et al., 2006). The present study quantified this reorganization in defined NTS subdivisions and demonstrated that CT fibers in the rostrolateral subdivision reorganize by retracting into a smaller region within the subdivision by losing axonal branches. A similar axonal retraction was not evident in the rostrocentral subdivision; neither the volume of the projections nor the CT fiber density within the rostrocentral subdivision changed during development. Thus, there is a selective retraction of axons, which undoubtedly is accompanied by synapse elimination in the rostrolateral subdivision. Furthermore, suggesting that rostrolateral CT axons are more susceptible for pathway reorganization, our results offer additional evidence for the differences between CT circuitries in rostrocentral and rostrolateral subdivisions.

In contrast to the rostrolateral subdivision, CT axons in the rostrocentral subdivision do not undergo pruning, although existing axons do modify synaptic connections.

Between P15 and P25, synapses redistribute among targets such that more of the CT input is poised to drive non-GABAergic cells rather GABAergic interneurons. In addition, another wave of reorganization, characterized by loss of synapses from existing branches, occurs after P35, resulting in a reduction of the CT contribution to rostrocentral circuitry. Thus, while CT circuitry undergoes a developmental reduction in both subdivisions, different mechanisms are employed: axon retraction in the rostrolateral subdivision and input reorganization in the rostrocentral subdivision.

Could developmental changes in the neuron morphology in the rostrocentral subdivision induce CT reorganization? That is, do developmental changes in postsynaptic targets drive presynaptic changes? Indeed, studies examining morphological development of both GABAergic and non-GABAergic circuitries indicate that some aspects of the rostrocentral circuitry continue to mature after P15. Although maturation of GABAergic soma ratios occurs before P15 in rat (Brown et al., 2000), a disproportionate reduction of non-GABAergic cells was noted after weaning (Brown et al., 2000). Similarly, a shift in GABAergic influences on gustatory neurons was noted after P15 in rat; sustained hyperpolarization responses following tetanic stimulation was diminished after P15 (Grabauskas and Bradley, 2001). Moreover, gustatory neurons in rat NTS undergo dendritic remodeling after the fourth postnatal week (Bao et al., 1995; Renehan et al., 1997), with a noticeable reduction in NTS cell dendritic branching. If young CT synapses were formed on the NTS cells that are remodeled after weaning, then the reduction of CT synapses could be explained by the late maturation of postsynaptic cells.

Our data provide further evidence for this mechanism by discounting other possibilities: CT synapse loss in the rostrocentral subdivision cannot be explained by an age-related pruning of presynaptic elements, similar to that seen in the neuromuscular junction and in the retinogeniculate pathway (Shatz and Kirkwood, 1984; Sanes and Lichtman, 1999; Hooks and Chen, 2006; Guido, 2008; Bickford et al., 2010; Speer et al., 2010). In these two systems, synaptic pruning is concurrent with structural maturation of terminals: prior to pruning, immature terminals display smaller terminal boutons and synaptic zones (Campbell and Shatz, 1992; Sanes and Lichtman, 1999). Furthermore, developmental axon pruning precedes terminal maturation by several weeks (Cragg, 1975; Shatz, 1996; Guido, 2008). In rat NTS, facial nerve axons prominently invade brain stem at E17–E19, without undergoing exuberance (Zhang and Ashwell, 2001). While these axons form synapses by birth, morphologically mature characteristics of NTS terminals, such as glomeruli and axo-spinous connections, are not present at these early postnatal ages (Whitehead, 1986; Zhang and Ashwell, 2001). In the current study we demonstrated that CT terminal morphology maturation is complete before P15 in both the rostrocentral and rostrolateral subdivisions. That is, the synaptic elimination and axon retraction observed in these subdivisions occur after CT terminals reach full morphological maturity. Furthermore, CT synapse reduction in rostrocentral subdivision seems to be due to selective loss of CT synapses, in addition to increase in neuropil volume.

Morphological and functional development of the NTS

The age-related pruning and reorganization of the CT input into the NTS occurs concomitantly with functional and anatomical changes resident to the CT and to the NTS. Although taste responses are present in the CT nerve at P15, when the terminal fields are large, mature taste responses are not apparent until about P35-P40 (Hill and Almli, 1980; Ferrell et al., 1981). Thus, maturation of functional responses at the nerve may drive the age-related retraction of CT terminal fields from rostrolateral subdivision, by emphasizing the gustatory activity relayed to rostrocentral NTS. By comparison, the functional maturation of cells postsynaptic to the CT in the rostrocentral NTS is more delayed; taste responses from single NTS neurons located in the rostrocentral subdivision to stimulation of the anterior tongue with salt stimuli increase in magnitude until about P60 (Hill et al., 1982, 1983), displaying at least 4× amplification in response magnitudes in NTS cells (Hill, 1987). This developmental time course is noticeably later than the time period when major reduction in CT fields was observed (that is, P15–P25), but it is consistent with the time course of the synaptic redistribution shown here for the rostrocentral subdivision. Furthermore, developmental changes in dendritic branching and spread of NTS neurons were also demonstrated (Lasiter et al., 1989; Bao et al., 1995; Renehan et al., 1997). These findings together suggest that synaptic reorganization at rostrocentral CT axons may be a refinement based on the maturation of postsynaptic cells, and that the developmental rearrangement of CT axons may be a refinement of functional synapses onto a subpopulation of NTS cells in the rostrocentral subdivision.

The subdivision-specific developmental alterations that we describe here for the CT nerve are undoubtedly intimately interrelated with the overall circuitry of the rostral NTS, thus having a widespread impact on the processing of orosensory signals. These functional changes may in turn have significant consequences on age-related behavioral taste preferences and aversions.

LITERATURE CITED

Bao H, Bradley RM, Mistretta CM. 1995. Development of intrinsic electrophysiological properties in neurons from the gustatory region of rat nucleus of solitary tract. Brain Res Dev Brain Res 86:143–154.

Bickford ME, Gunluk AE, Van Horn SC, Sherman SM. 1994. GABAergic projection from the basal forebrain to the visual sector of the thalamic reticular nucleus in the cat. J Comp Neurol 348:481–510.

Bickford ME, Slusarczyk A, Dilger EK, Krahe TE, Kucuk C, Guido W. 2010. Synaptic development of the mouse dorsal lateral geniculate nucleus. J Comp Neurol 518:622–635.

Biedenbach MA, Chan KY. 1971. Tongue mechanoreceptors: comparison of afferent fibers in the lingual nerve and chorda tympani. Brain Res 35:584–588.

Brown M, Renehan WE, Schweitzer L. 2000. Changes in GABA-immunoreactivity during development of the rostral subdivision of the nucleus of the solitary tract. Neuroscience 100:849–859.

Campbell G, Shatz CJ. 1992. Synapses formed by identified retinogeniculate axons during the segregation of eye input. J Neurosci 12:1847–1858.

Colman H, Nabekura J, Lichtman JW. 1997. Alterations in synaptic strength preceding axon withdrawal. Science 275: 356–361.

Corson SL, Hill DL. 2011. Chorda tympani nerve terminal field maturation and maintenance is severely altered following changes to gustatory nerve input to the nucleus of the solitary tract. J Neurosci 31:7591–603

Corson J, Aldridge A, Wilmoth K, Erisir A. 2012. A survey of oral cavity afferents to the rat nucleus tractus solitarii. J Comp Neurol 520:495–527.

Costen JB, Clare MH, Bishop GH. 1951. The transmission of pain impulses via the chorda tympani nerve. Ann Otol Rhinol Laryngol 60:591–609.

Cragg BG. 1975. The development of synapses in the visual system of the cat. J Comp Neurol 160:147–166

DeFelipe J, Marco P, Busturia I, Merchan-Perez A. 1999. Estimation of the number of synapses in the cerebral cortex: methodological considerations. Cereb Cortex 9:722–732.

Demas J, Sagdullaev BT, Green E, Jaubert-Miazza L, McCall MA, Gregg RG, Wong RO, Guido W. 2006. Failure to maintain eye-specific segregation in nob, a mutant with abnormally patterned retinal activity. Neuron 50:247–259.

Erickson R. 1966. Nontraumatic headholders for mammals. Physiol Behav 1:97–98.

Erisir A, Dreusicke M. 2005. Quantitative morphology and postsynaptic targets of thalamocortical axons in critical period and adult ferret visual cortex. J Comp Neurol 485: 11–31.

Erisir A, Harris JL. 2003. Decline of the critical period of visual plasticity is concurrent with the reduction of NR2B subunit of the synaptic NMDA receptor in layer 4. J Neurosci 23: 5208–5218.

Erisir A, Van Horn SC, Bickford ME, Sherman SM. 1997. Immunocytochemistry and distribution of parabrachial terminals in the lateral geniculate nucleus of the cat: a comparison with corticogeniculate terminals. J Comp Neurol 377:535–549.

Farbman AI, Hellekant G. 1978. Quantitative analyses of the fiber population in rat chorda tympani nerves and fungiform papillae. Am J Anat 153:509–521.

Ferrell MF, Mistretta CM, Bradley RM. 1981. Development of chorda tympani taste responses in rat. J Comp Neurol 198:37–44.

Grabauskas G, Bradley RM. 2001. Postnatal development of inhibitory synaptic transmission in the rostral nucleus of the solitary tract. J Neurophysiol 85:2203–2212.

Guido W. 2008. Refinement of the retinogeniculate pathway. J Physiol 586(Pt 18):4357–4362.

Halsell CB, Travers SP. 1997. Anterior and posterior oral cavity responsive neurons are differentially distributed among parabrachial subnuclei in rat. J Neurophysiol 78:920–938.

Halsell CB, Travers SP, Travers JB. 1996. Ascending and descending projections from the rostral nucleus of the solitary tract originate from separate neuronal populations. Neuroscience 72:185–197.

Harada S, Yamamoto T, Yamaguchi K, Kasahara Y. 1997. Different characteristics of gustatory responses between the greater superficial petrosal and chorda tympani nerves in the rat. Chem Sens 22:133–140.

Herbert H, Moga MM, Saper CB. 1990. Connections of the parabrachial nucleus with the nucleus of the solitary tract and the medullary reticular formation in the rat. J Comp Neurol 293:540–580.

Hill DL. 1987. Development of taste responses in the rat parabrachial nucleus. J Neurophysiol 57:481–495.

Hill DL, Almli CR. 1980. Ontogeny of chorda tympani nerve responses to gustatory stimuli in the rat. Brain Res 197: 27–38.

Hill DL, Mistretta CM, Bradley RM. 1982. Developmental changes in taste response characteristics of rat single chorda tympani fibers. J Neurosci 2:782–790.

Hill DL, Bradley RM, Mistretta CM. 1983. Development of taste responses in rat nucleus of solitary tract. J Neurophysiol 50:879–895.

Holland GR, Robinson PP. 1992. Axon populations in cat lingual and chorda tympani nerves. J Dent Res 71: 1468–1472.

Hooks BM, Chen C. 2006. Distinct roles for spontaneous and visual activity in remodeling of the retinogeniculate synapse. Neuron 52:281–291.

Inan M, Crair MC. 2007. Development of cortical maps: perspectives from the barrel cortex. Neuroscientist 13:49–61.

Kamiyama T, Yoshioka N, Sakurai M. 2006. Synapse elimination in the corticospinal projection during the early postnatal period. J Neurophysiol 95:2304–2313.

Kasthuri N, Lichtman JW. 2003. The role of neuronal identity in synaptic competition. Nature 424:426–430.

Katz LC, Shatz CJ. 1996. Synaptic activity and the construction of cortical circuits. Science 274:1133–1138.

King CT, Hill DL. 1991. Dietary sodium chloride deprivation throughout development selectively influences the terminal field organization of gustatory afferent fibers projecting to the rat nucleus of the solitary tract. J Comp Neurol 303: 159–169.

Krimm RF, Hill DL. 1997. Early prenatal critical period for chorda tympani nerve terminal field development. J Comp Neurol 378:254–264.

Lasiter PS, Wong DM, Kachele DL. 1989. Postnatal development of the rostral solitary nucleus in rat: dendritic morphology and mitochondrial enzyme activity. Brain Res Bull 22:313–321.

Lundy RF Jr, Contreras RJ. 1999. Gustatory neuron types in rat geniculate ganglion. J Neurophysiol 82:2970–2988.

Luo L, O'Leary DD. 2005. Axon retraction and degeneration in development and disease. Annu Rev Neurosci 28: 127–156.

Mangold JE, Hill DL. 2007. Extensive reorganization of primary afferent projections into the gustatory brainstem induced by feeding a sodium-restricted diet during development: less is more. J Neurosci 27:4650–4662.

Mangold JE, Hill DL. 2008. Postnatal reorganization of primary afferent terminal fields in the rat gustatory brainstem is determined by prenatal dietary history. J Comp Neurol 509:594–607.

Matsuo R, Inoue T, Masuda Y, Nakamura O, Yamauchi Y, Morimoto T. 1995. Neural activity of chorda tympani mechanosensitive fibers during licking behavior in rats. Brain Res 689:289–298.

May OL, Hill DL. 2006. Gustatory terminal field organization and developmental plasticity in the nucleus of the solitary tract revealed through triple-fluorescence labeling. J Comp Neurol 497:658–669.

May OL, Erisir A, Hill DL. 2007. Ultrastructure of primary afferent terminals and synapses in the rat nucleus of the solitary tract: comparison among the greater superficial petrosal, chorda tympani, and glossopharyngeal nerves. J Comp Neurol 502:1066–1078.

May OL, Erisir A, Hill DL. 2008. Modifications of gustatory nerve synapses onto nucleus of the solitary tract neurons induced by dietary sodium-restriction during development. J Comp Neurol 508:529–541.

McLaughlin T, Torborg CL, Feller MB, O'Leary DD. 2003. Retinotopic map refinement requires spontaneous retinal waves during a brief critical period of development. Neuron 40:1147–1160.

Nejad MS. 1986. The neural activities of the greater superficial petrosal nerve of the rat in response to chemical stimulation of the palate. Chem Sens 11:283–293.

Ninomiya Y. 1996. Salt taste responses of mouse chorda tympani neurons: evidence for existence of two different amiloride-sensitive receptor components for NaCl with different temperature dependencies. J Neurophysiol 76: 3550–3554.

Norgren R. 1978. Projections from the nucleus of the solitary tract in the rat. Neuroscience 3:207–218.

Norgren R, Leonard CM. 1973. Ascending central gustatory pathways. J Comp Neurol 150:217–237.

O'Leary DD, Bicknese AR, De Carlos JA, Heffner CD, Koester SE, Kutka LJ, Terashima T. 1990. Target selection by cortical axons: alternative mechanisms to establish axonal connections in the developing brain. Cold Spring Harb Symp Quant Biol 55:453–468.

O'Leary DD, Schlaggar BL, Stanfield BB. 1992. The specification of sensory cortex: lessons from cortical transplantation. Exp Neurol 115:121–126.

Ogawa H, Sato M, Yamashita S. 1968. Multiple sensitivity of chordat typani fibres of the rat and hamster to gustatory and thermal stimuli. J Physiol 199:223–240.

Penn AA, Shatz CJ. 1999. Brain waves and brain wiring: the role of endogenous and sensory-driven neural activity in development. Pediatr Res 45(4 Pt 1):447–458.

Perez R, Fuoco G, Dorion JM, Ho PH, Chen JM. 2006. Does the chorda tympani nerve confer general sensation from the tongue? Otolaryngol Head Neck Surg 135:368–373.

Phend KD, Weinberg RJ, Rustioni A. 1992. Techniques to optimize post-embedding single and double staining for amino acid neurotransmitters. J Histochem Cytochem 40:1011–1020.

Renehan WE, Massey J, Jin Z, Zhang X, Liu YZ, Schweitzer L. 1997. Developmental changes in the dendritic architecture of salt-sensitive neurons in the nucleus of the solitary tract. Brain Res Dev Brain Res 102:231–246.

Sanes JR, Lichtman JW. 1999. Development of the vertebrate neuromuscular junction. Annu Rev Neurosci 22:389–442.

Schmued LC. 1990. A rapid, sensitive histochemical stain for myelin in frozen brain sections. J Histochem Cytochem 38: 717–720.

Schmued L, Slikker W Jr. 1999. Black-gold: a simple, high-resolution histochemical label for normal and pathological myelin in brain tissue sections. Brain Res 837:289–297.

Shatz CJ. 1996. Emergence of order in visual system development. Proc Natl Acad Sci U S A 93:602–608.

Shatz CJ, Kirkwood PA. 1984. Prenatal development of functional connections in the cat's retinogeniculate pathway. J Neurosci 4:1378–1397.

Smith KG, Yates JM, Robinson PP. 2004. The effect of nerve growth factor on functional recovery after injury to the chorda tympani and lingual nerves. Brain Res 1020:62–72.

Sollars SI, Hill DL. 2005. In vivo recordings from rat geniculate ganglia: taste response properties of individual greater superficial petrosal and chorda tympani neurones. J Physiol 564(Pt 3):877–893.

Sollars SI, Walker BR, Thaw AK, Hill DL. 2006. Age-related decrease of the chorda tympani nerve terminal field in the nucleus of the solitary tract is prevented by dietary sodium restriction during development. Neuroscience 137: 1229–1236.

Speer CM, Mikula S, Huberman AD, Chapman B. 2010. The developmental remodeling of eye-specific afferents in the ferret dorsal lateral geniculate nucleus. Anat Rec (Hoboken) 293:1–24.

Tamamaki N, Yanagawa Y, Tomioka R, Miyazaki JI, Obata K, Kaneko T. 2003. Green fluorescent protein expression and colocalization with calretinin, parvalbumin, and somatostatin in the GAD67-GFP knock-in mouse. J Comp Neurol 467:60–79.

Wang M, Bradley RM. 2010. Properties of GABAergic neurons in the rostral solitary tract nucleus in mice. J Neurophysiol 103:3205–3218.

Whitehead MC. 1986. Anatomy of the gustatory system in the hamster: synaptology of facial afferent terminals in the solitary nucleus. J Comp Neurol 244:72–85.

Whitehead MC. 1990. Subdivisions and neuron types of the nucleus of the solitary tract that project to the parabrachial nucleus in the hamster. J Comp Neurol 301: 554–574.

Whitehead MC, Ganchrow JR, Ganchrow D, Yao B. 1999. Organization of geniculate and trigeminal ganglion cells innervating single fungiform taste papillae: a study with tetramethylrhodamine dextran amine labeling. Neuroscience 93:931–941.

Whiteside B. 1927. Nerve overlap in the gustatory apparatus of the rat. J Comp Neurol 44:363–377.

Zhang LL, Ashwell KW. 2001. The development of cranial nerve and visceral afferents to the nucleus of the solitary tract in the rat. Anat Embryol 204:134–51

Ziburkus J, Guido W. 2006. Loss of binocular responses and reduced retinal convergence during the period of retinogeniculate axon segregation. J Neurophysiol 96:2775–2784.